fluids

MDPI

Article

Numerical Investigation of Stall Flutter of a Pitching Airfoil at Low Reynolds Number

Maria Adele Cecchini [1], Giulio Soldati [1], Peter Jordan [2] and Sergio Pirozzoli [1,*]

[1] Dipartimento di Ingegneria Meccanica e Aerospaziale, Sapienza Università di Roma, Via Eudossiana 18, 00184 Roma, Italy; giulio.soldati@uniroma1.it (G.S.)
[2] Institut PPRIME, CNRS—Université de Poitiers—ISAE-ENSMA, 86961 Chasseneuil, France
* Correspondence: sergio.pirozzoli@uniroma1.it

Abstract

The present work investigates fluid–structure instabilities and flow-induced oscillations of a pitching NACA0012 airfoil through numerical simulations. The flow is modeled using the compressible Navier–Stokes equations in a non-inertial rotating reference frame, while the structural dynamics are represented by a torsional spring–mass–damper system. The analysis focuses on the effects of reduced velocity, equilibrium angle of attack, and elastic axis position on the aeroelastic behavior at low Reynolds number ($Re = 1000$). Particular attention is devoted to characterizing the transition from vortex-shedding-dominated oscillations to fully developed limit-cycle oscillations and to assessing its sensitivity to aerodynamic and structural parameters. The results show a transition from steady flow to vortex shedding and, at higher reduced velocities, to limit-cycle oscillations. Increasing the equilibrium angle of attack promotes an earlier onset of instability and stronger aerodynamic forcing, while moving the elastic axis downstream has a similar destabilizing effect due to the larger aerodynamic moment arm (up to approximately 20% reduction of the critical reduced velocity). The nature of the transition is found to depend strongly on the equilibrium angle of attack, with distinct behaviors observed at low and high incidence. Frequency analysis highlights the progressive coupling between fluid and structural dynamics: vortex shedding dominates in the weakly coupled regime, whereas the structural frequency governs the response in the limit-cycle regime. The study provides a consistent description of the mechanisms driving flow-induced oscillations and of the parameters controlling aeroelastic stability.

Keywords: flow-induced oscillations; aeroelastic response; frequency analysis

Check for updates

Academic Editor: Tian Li

Received: 15 May 2026
Revised: 5 June 2026
Accepted: 8 June 2026
Published: 11 June 2026

Copyright: © 2026 by the authors. Licensee MDPI, Basel, Switzerland. This article is an open access article distributed under the terms and conditions of the Creative Commons Attribution (CC BY) license.

1. Introduction

Fluid–structure interaction (FSI) phenomena arise in a wide range of natural and engineering systems, where the coupling between aerodynamic loads and structural dynamics can lead to complex and potentially unstable behavior. Examples include biological systems, such as the vibration of vocal cords and animal locomotion, as well as engineering applications involving flexible structures interacting with a surrounding fluid. In aeronautical applications, aeroelastic instabilities such as flutter represent a critical design constraint, as they may compromise structural integrity and must be avoided within the operational envelope [1]. Despite almost a century of research, flutter prediction remains an active area of investigation, particularly in the presence of nonlinear aerodynamic and structural effects [2]. At the same time, controlled fluid–structure coupling is increasingly exploited

in modern configurations, including flexible and morphing wings, where aeroelastic effects can enhance aerodynamic performance.

Flutter is fundamentally governed by the interaction between unsteady aerodynamic forces and structural dynamics. In its simplest form, the problem can be interpreted as a competition between structural and flow time scales [3]. The structural response is characterized by its natural frequency and damping, while the flow introduces additional time scales associated with separation, vortex formation, and reattachment. Their interaction may lead to self-sustained oscillations when the aerodynamic energy input overcomes structural dissipation. The nonlinear development of aeroelastic instabilities often leads to the emergence of limit-cycle oscillations, whose accurate prediction remains a central challenge in aeroelastic analyses, especially for high-degree-of-freedom systems [4].

At low Reynolds numbers, the role of flow separation and dynamic stall becomes particularly important, leading to strongly nonlinear behavior. Recent studies have also explored the modeling of unsteady aerodynamic loads on oscillating airfoils through both high-fidelity simulations and data-driven reduced-order models. For instance, Baldan and Guardone [5] developed a machine-learning framework for predicting aerodynamic loads on pitching NACA0012 airfoils undergoing light and deep dynamic stall, highlighting the importance of accurately capturing nonlinear aerodynamic phenomena in aeroelastic applications. In these regimes, the aeroelastic response is often characterized by large-amplitude limit-cycle oscillations (LCO), hysteresis and complex bifurcation structures that cannot be described by linear theory. Understanding the mechanisms governing these regimes is therefore essential for predicting and controlling aeroelastic instabilities.

The unsteady aerodynamics of pitching airfoils under prescribed motion has been extensively investigated to characterize separation dynamics and vortex evolution. It has been shown that the development of boundary layer separation depends sensitively on reduced frequency [6–8], while the Reynolds number effects significantly influence aerodynamic loads [9]. More recent studies have further clarified the reattachment process in dynamic stall conditions, highlighting the presence of multiple temporal stages [10].

Although prescribed-motion studies are fundamental for understanding the underlying aerodynamic mechanisms, recent investigations have shown that aeroelastic stall-flutter simulations require stricter numerical requirements than static or forced-motion airfoil calculations [11]. Thus, in parallel, flow-induced oscillations of elastically supported airfoils have been widely studied. Several studies have focused on two-degree-of-freedom aeroelastic systems, in which the airfoil is free to both pitch and plunge [12,13]. For example, Kumar et al. [14] experimentally investigated the influence of preset angles and frequency ratios on airfoil behavior, highlighting bifurcation characteristics and synchronization mechanisms of the aeroelastic response. Other studies have considered simplified configurations, typically consisting of a rigid airfoil mounted on a torsional spring–damper system [15,16]. Despite their apparent simplicity, such systems exhibit rich nonlinear dynamics. Both experimental and numerical investigations have reported self-sustained oscillations at transitional Reynolds numbers [17,18], while cyber–physical experiments and numerical studies have demonstrated the strong sensitivity of the aeroelastic response to both structural and aerodynamic parameters [19,20].

A common interpretation emerging from these studies is that flutter can be described in terms of the energy exchange between the fluid and the structure. Oscillations grow when the net aerodynamic work over one cycle exceeds structural dissipation and saturate when the two contributions balance. This perspective has been formalized through energy-based approaches, including the concept of energy maps for forced oscillations [3] and more recent extensions to stall-flutter prediction and control [21,22]. Although most research

efforts focus on predicting or suppressing flutter, there is also considerable interest in exploiting flow-induced oscillations for energy harvesting applications [19,23].

In this work, we investigate flow-induced pitch oscillations of a rigid NACA0012 airfoil elastically supported by a linear torsional spring and damper. The analysis is conducted at a low Reynolds number ($Re = 1000$), where nonlinear flow phenomena can be examined in detail. The coupled fluid–structure system is solved numerically using the Navier–Stokes equations formulated in a rotating reference frame, together with a single-degree-of-freedom structural model. The study is restricted to a single low-Mach-number condition ($M = 0.2$) representative of incompressible flow. A dedicated assessment of Mach-number effects is beyond the scope of the present work and is left for future investigation.

After verification and validation of the numerical framework, we investigate the influence of reduced velocity, equilibrium angle of attack, and elastic-axis position on the aeroelastic response. Particular attention is devoted to the transition from a vortex-shedding-dominated response to fully coupled limit-cycle oscillations and to the identification of the distinct dynamical regimes that emerge as the governing parameters are varied. The objective is to characterize the mechanisms controlling instability onset, oscillation amplitude, and frequency selection and to clarify how aerodynamic and structural time scales interact across the different response regimes. Although the present study is restricted to low Reynolds numbers, the results provide insight into the fundamental mechanisms governing flow-induced oscillations and fluid–structure coupling, which are relevant to more complex aeroelastic systems.

The low-Reynolds-number regime considered here allows a clearer investigation of the fundamental mechanisms governing fluid–structure interaction and aeroelastic instability onset. Recent studies have highlighted the importance of accurately capturing flow separation, laminar separation-bubble dynamics, and wake instabilities in oscillating airfoils [24,25]. The subsequent formation and evolution of leading-edge vortices play a central role in determining the unsteady aerodynamic loads and the resulting aeroelastic response [26]. Although the present results are restricted to low Reynolds numbers, they provide insight into physical mechanisms that are expected to remain relevant at higher Reynolds numbers, even though the quantitative characteristics of the response may differ substantially.

2. Numerical Setup

We consider a two-dimensional NACA0012 airfoil immersed in a uniform flow of free-stream velocity u_0. The airfoil is allowed to rotate about a prescribed elastic axis and is analyzed within a non-inertial reference frame rigidly attached to the body, as schematically shown in Figure 1. This formulation allows the airfoil to remain fixed in the computational domain, while its motion is accounted for through additional source terms in the governing equations. The flow is solved using a compressible formulation, consistent with the numerical solver employed in the present study. Under the present conditions, with free-stream Mach number $M = 0.2$, compressibility effects are expected to remain weak, and the flow may be regarded as effectively incompressible. The use of a compressible solver nevertheless provides a unified framework that can be readily extended to higher Mach numbers in future investigations.

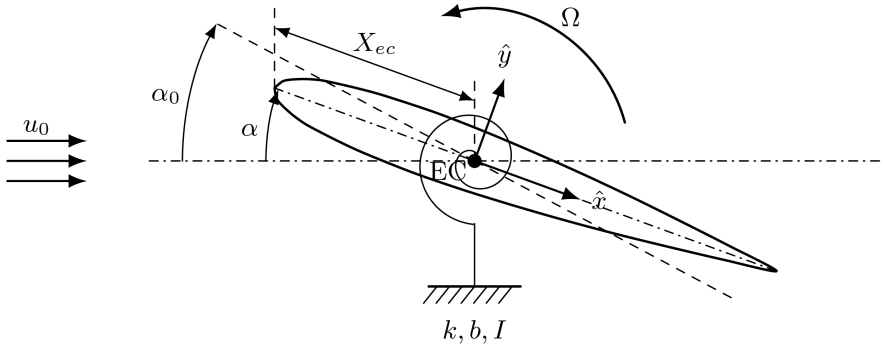


Figure 1. Schematic representation of the aeroelastic configuration. A NACA0012 airfoil is immersed in a uniform free stream of velocity u_0 and is allowed to rotate about the elastic center (EC). The airfoil is supported by a torsional spring–damper–inertia system characterized by stiffness k, damping b, and moment of inertia I. The instantaneous incidence angle is denoted by α, while α_0 represents the equilibrium incidence angle. The elastic-axis location is specified through the distance X_{ec} between the leading edge and the elastic center. The body-fixed rotating reference frame $(\hat{x}, \hat{y})$ rotates with angular velocity Ω.

The aerodynamic field is described by the compressible Navier–Stokes equations expressed in the rotating frame. In terms of relative variables, the conservation of mass reads

$$\frac{\partial \hat{\rho}}{\partial t} + \nabla \cdot (\hat{\rho}\hat{\boldsymbol{u}}) = 0, \tag{1}$$

where the hat symbol denotes the quantities in the rotating frame. The momentum equation is written as

$$\frac{\partial (\hat{\rho}\hat{\boldsymbol{u}})}{\partial t} = -\nabla \cdot (\hat{\rho}\hat{\boldsymbol{u}} \otimes \hat{\boldsymbol{u}}) - \nabla \hat{p} + \nabla \cdot \hat{\boldsymbol{\sigma}} + \underbrace{2\hat{\rho}\hat{\boldsymbol{u}} \times \boldsymbol{\Omega} - \hat{\rho}\boldsymbol{\Omega} \times (\boldsymbol{\Omega} \times \hat{\boldsymbol{x}}) + \hat{\rho}\dot{\boldsymbol{\Omega}} \times \hat{\boldsymbol{x}}}_{\boldsymbol{f}_{\text{rot}}}, \tag{2}$$

where $\boldsymbol{\Omega} \equiv (0, 0, \Omega)$ is the angular velocity vector, $\hat{\boldsymbol{x}} \equiv (\hat{x}, \hat{y}, 0)$ is the position vector in the rotating frame and $\boldsymbol{f}_{\text{rot}}$ includes the apparent forces (namely Coriolis, centrifugal and Euler forces) arising from the non-inertial formulation. The viscous stress tensor is defined as

$$\hat{\boldsymbol{\sigma}} = \hat{\mu}\left(\nabla \hat{\boldsymbol{u}} + \nabla \hat{\boldsymbol{u}}^T\right) - \frac{2}{3}\hat{\mu}(\nabla \cdot \hat{\boldsymbol{u}})\boldsymbol{I}. \tag{3}$$

The total energy equation reads

$$\frac{\partial (\hat{\rho}\hat{E})}{\partial t} = -\nabla \cdot (\hat{\rho}\hat{\boldsymbol{u}}\hat{H}) + \nabla \cdot (\hat{\boldsymbol{\sigma}} \cdot \hat{\boldsymbol{u}}) - \nabla \cdot \hat{\boldsymbol{q}} + \boldsymbol{f}_{\text{rot}} \cdot \hat{\boldsymbol{u}}, \tag{4}$$

where $\hat{\boldsymbol{q}} = -\hat{k}\nabla \hat{T}$, and $\boldsymbol{f}_{\text{rot}} \cdot \hat{\boldsymbol{u}}$ is the power density of non-inertial forces. The velocity in the rotating frame is related to the absolute velocity through

$$\hat{\boldsymbol{u}} = \boldsymbol{u} - \boldsymbol{\Omega} \times \boldsymbol{r}. \tag{5}$$

The system is closed using the perfect gas law and Sutherland's law for viscosity.

The airfoil is elastically supported by a torsional spring–damper system, providing a single rotational degree of freedom, as illustrated in Figure 1. The structural dynamics are governed by

$$I^*\ddot{\alpha} + b^*\dot{\alpha} + k^*(\alpha - \alpha_0) = C_m, \tag{6}$$

where $I^* = 2I/(\rho c^4)$, $b^* = 2b/(\rho u_0 c^3)$, and $k^* = 2k/(\rho {u_0}^2 c^2)$ are the non-dimensional inertia, damping, and stiffness coefficients, $C_m = M/(0.5\rho {u_0}^2 c^3)$ is the aerodynamic moment coefficient with respect to the elastic axis position (X_{ec}), c is the airfoil chord, α is the instantaneous angle of attack, and α_0 is the equilibrium angular position of the airfoil. The damping is also expressed through the non-dimensional damping ratio

$$\zeta^* = \frac{b}{2\sqrt{kI}}. \tag{7}$$

The aeroelastic response is characterized by the reduced velocity

$$U^* = \frac{u_0}{f_n c}, \tag{8}$$

and the natural structural frequency

$$f_n = \frac{1}{2\pi}\sqrt{\frac{k}{I}}. \tag{9}$$

The coupled fluid–structure system is obtained by solving the flow equations together with the structural dynamics, where the aerodynamic moment acts as the forcing term driving the airfoil motion.

3. Numerical Method

The governing equations are discretized using a finite volume method on a structured body-fitted grid. The conservative form of the compressible Navier–Stokes equations is integrated over each control volume. Convective fluxes are evaluated using a central differencing scheme stabilized through the triple-splitting formulation proposed by Pirozzoli [27,28], Soldati et al. [29], which preserves the overall kinetic energy in the discrete limit of inviscid incompressible flow. Viscous fluxes are discretized using second-order central differences. Time integration is performed using an explicit third-order Runge–Kutta scheme. The time step is dynamically adjusted to maintain a CFL number equal to 0.2. The source terms associated with the rotating reference frame are explicitly included in the residual evaluation, ensuring consistency between the flow solution and the airfoil motion.

Boundary conditions are defined consistently with the rotating reference-frame formulation. At the airfoil surface, a no-slip condition is enforced, corresponding to zero relative velocity in the rotating frame. At the far-field boundaries, free-stream conditions are imposed using velocity components expressed in the rotating frame. To avoid spurious reflections at the outer boundaries, a sponge layer is introduced in the far-field region. Within this region, the flow variables are gradually relaxed toward free-stream conditions through a spatially varying damping coefficient. The damping intensity increases smoothly with radial distance from the airfoil, ensuring a continuous transition between the inner computational domain and the outer boundary. Each simulation was continued until a statistically stationary regime was reached. Stationarity was assessed from the convergence of both the oscillation amplitude and the dominant frequency over a sufficiently long observation interval, corresponding to at least 50% of the total signal duration. Statistical quantities and spectral analyses were subsequently computed using only the stationary portion of the signal, after removal of the initial transient.

The computational domain is discretized using a structured C-type mesh around the airfoil, as shown in Figure 2. This configuration allows accurate resolution of the boundary layer along the airfoil surface and an appropriate representation of the wake region.

The grid is generated by rotating the airfoil geometry according to the prescribed equilibrium angle of attack (α_0), ensuring alignment between the mesh and the flow

configuration. Grid spacing is refined near the airfoil surface to resolve boundary-layer gradients, while a gradual coarsening is applied in the far-field and wake regions through a geometric progression to reduce the computational cost. The overall resolution is selected to achieve a balance between accuracy and efficiency while maintaining smooth grid transitions and avoiding excessive stretching ratios. All meshes were generated using the same wall-normal clustering strategy. The first grid point adjacent to the airfoil surface was located approximately $0.01c$ away from the wall, ensuring adequate resolution of the near-wall viscous region. The computational domain extends to an outer radius of $25\,c$ from the airfoil.

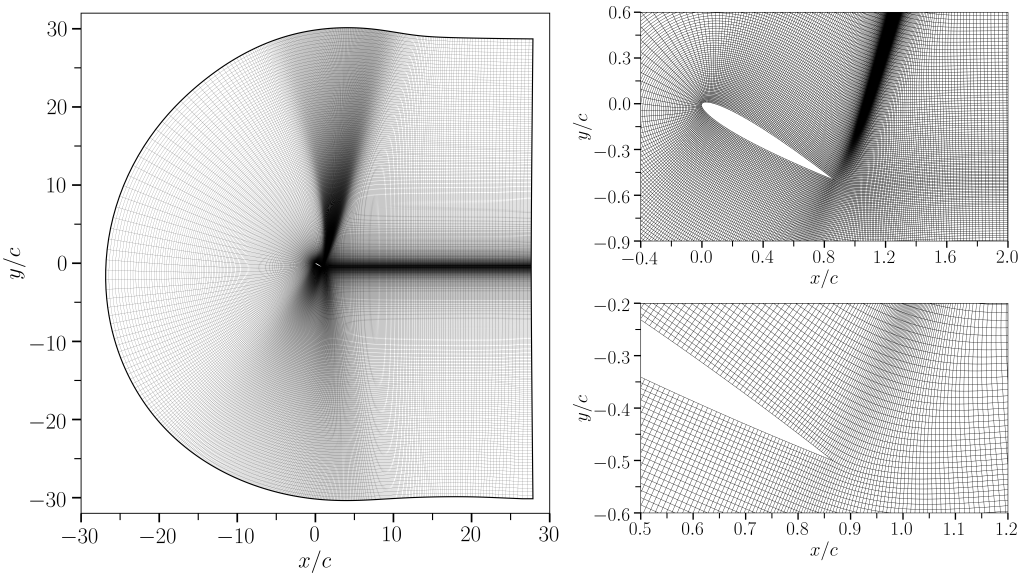
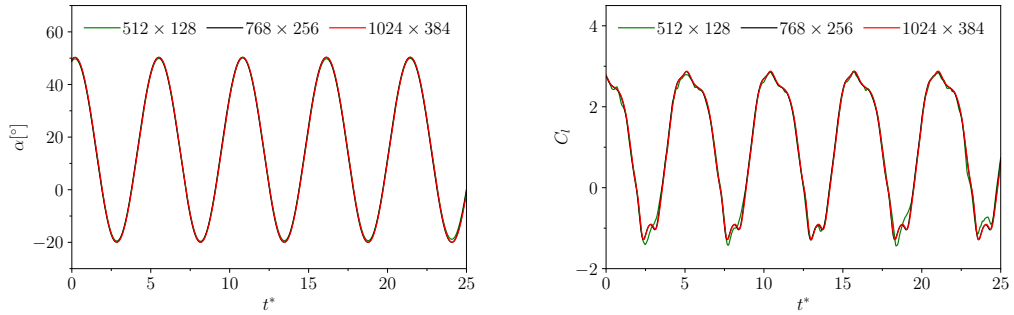


Figure 2. Computational grid. (**Left**): Global view of the two-dimensional computational domain. (**Right**): Detailed views near the airfoil (**top**) and near the trailing edge (**bottom**).

4. Verification and Validation

A grid-convergence study is performed to assess the sensitivity of the solution to spatial resolution, as shown in Figure 3. Three structured grids of increasing resolution are considered, and the resulting time histories of the angle of attack and lift coefficient are compared. Unless otherwise specified, all time series reported in the present study are shown as a function of the dimensionless time $t^* = (t - t_0), u_0/c$, where t_0 denotes the end of the initial transient interval.



(**a**) (**b**)

Figure 3. Time evolution of the angle of attack (**a**) and lift coefficient (**b**) obtained using three grids of increasing resolution.

In addition, several metrics are evaluated and reported in Tables 1 and 2, together with their relative differences with respect to the finest grid. These include the mean angle of attack $\bar{\alpha}$, mean aerodynamic moment coefficient $\bar{C}_m$, and mean lift coefficient $\bar{C}_l$, as well as the corresponding oscillation amplitudes A_α, A_m, and A_l. The dominant Strouhal number, St_l, obtained from the spectral analysis of the lift coefficient, is also reported.

Table 1. Quantitative results of the grid-convergence study. Reported quantities include the mean values and oscillation amplitudes of the angle of attack, moment coefficient, and lift coefficient, together with the dominant Strouhal number extracted from the lift signal.

Resolution	$\bar{\alpha}$ [°]	A_α [°]	$\bar{C}_m$	A_m	$\bar{C}_l$	A_l	St_l
512 × 128	14.869	9.718	−0.0570	0.475	1.126	2.215	0.0667
768 × 256	14.256	9.825	−0.0437	0.468	1.066	2.080	0.0656
1024 × 384	14.188	9.822	−0.0321	0.467	1.488	2.084	0.0656

Table 2. Relative differences with respect to the finest grid (1024 × 384) for the quantities reported in Table 1. Reported values include the relative differences in the oscillation amplitudes of the angle of attack, moment coefficient, and lift coefficient, together with the dominant Strouhal number extracted from the lift signal.

Resolution	ΔA_α (%)	ΔA_m (%)	ΔA_l (%)	ΔSt_l (%)
512 × 128	−1.06	1.7	6.28	1.67
768 × 256	0.03	0.21	−0.19	0.03

The quantitative results confirm the trends observed in Figure 3. Relative to the finest-grid solution, the intermediate grid predicts the oscillation amplitude of the angle of attack with an error of only 0.03%, while the amplitudes of the moment and lift coefficients differ by less than 0.2%. The relative difference in the dominant Strouhal number is below 0.1%. These results indicate that the intermediate grid provides a solution that is essentially indistinguishable from the finer grid, while significantly reducing the computational cost. This grid is therefore adopted for all subsequent simulations. The selected grid consists of 256 nodes in the wall-normal direction and 768 nodes in the wall-parallel direction, distributed over 256 nodes along the airfoil surface and 512 nodes in the wake region. The corresponding streamwise grid spacing along the airfoil is approximately $\Delta x = 0.005\,c$.

The correctness of the structural model implementation is verified by considering the case without aerodynamic forcing, for which an analytical solution is available. In this limit, the governing equation reduces to a damped harmonic oscillator.

The numerical results are in perfect agreement with the analytical solution, as shown in Figure 4, thereby confirming the correct implementation of the structural dynamics.

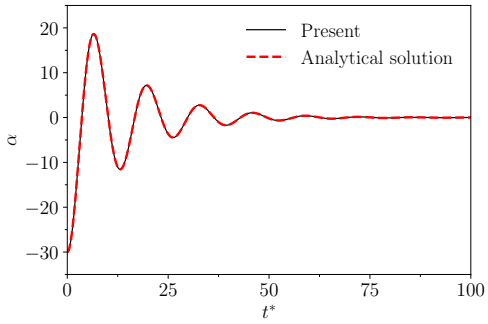
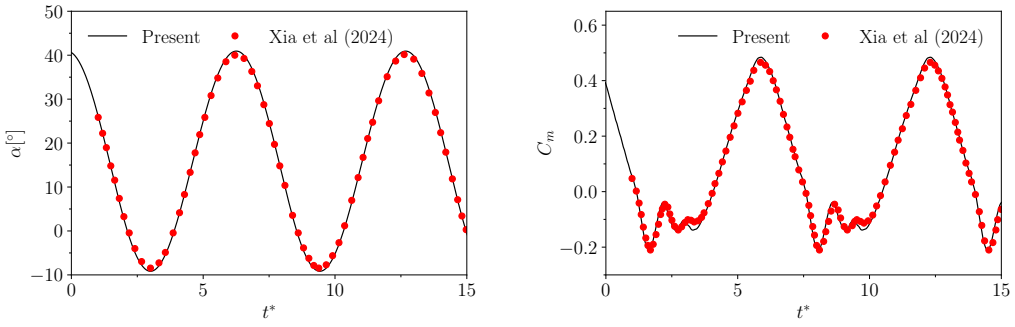


Figure 4. Time evolution of the angle of attack for the unforced structural response obtained from the numerical simulation and compared with the analytical solution.

Regarding the flow-induced dynamics, a comparison is carried out with the results obtained by Xia et al. [21] for the case with $\zeta^* = 0.03$, $X_{ec}{}^* = X_{ec}/c = 0.5$, $I^* = 4.5$, $Re = 1000$, $M = 0.1$, and $U^* = 6$. As shown in Figure 5, the present results are in good agreement with those reported in the reference paper.



(**a**) (**b**)

Figure 5. Time evolution of the angle of attack (**a**) and moment coefficient (**b**) obtained from the numerical simulation and compared with the results reported by Xia et al. [21].

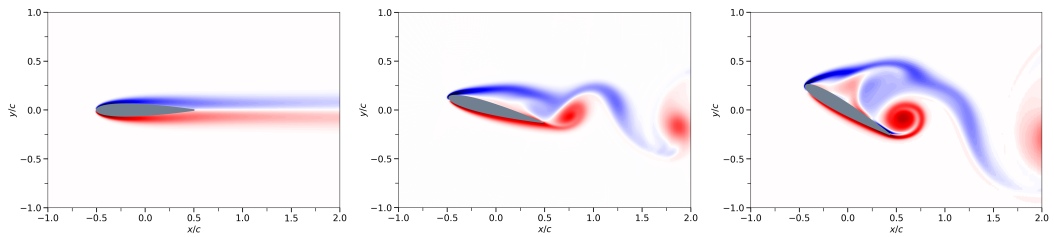
The numerical results reproduce both the amplitude and temporal evolution of the oscillations with good accuracy, demonstrating the capability of the solver to capture the coupled aeroelastic dynamics.

5. Results

5.1. Flow Regimes for the Rigid Airfoil

The aerodynamic response of the rigid airfoil is first analyzed in order to characterize the baseline flow behavior in the absence of structural coupling. Three equilibrium angles of attack are considered, namely, $\alpha_0 = 0°$, 15°, and 30°.

As shown in Figure 6, the flow undergoes a clear transition with increasing equilibrium angle of attack. At $\alpha_0 = 0°$, the flow remains steady and symmetric, with no evidence of vortex shedding. At $\alpha_0 = 15°$, periodic vortex shedding develops, associated with a coherent separated shear layer. At $\alpha_0 = 30°$, the flow becomes strongly separated and exhibits more complex and irregular vortex dynamics, indicative of a nonlinear regime. This transition is further quantified through frequency analysis of the aerodynamic loads. The frequency response is expressed in terms of the Strouhal number, $St = fc/u_0$, where f is the dominant frequency extracted from the signals of C_M and C_L. Figures 7 and 8 show the corresponding time histories and power spectral densities, respectively.



(**a**) (**b**) (**c**)

Figure 6. Instantaneous vorticity fields for increasing equilibrium angles of attack: (**a**) $\alpha_0 = 0°$, (**b**) $\alpha_0 = 15°$, and (**c**) $\alpha_0 = 30°$. The vorticity field is rendered in a colour scale ranging from blue (negative values) to red (positive values).

At $\alpha_0 = 0°$, no dominant frequency is observed, confirming the steady nature of the flow. For $\alpha_0 = 15°$, a clear peak appears at a characteristic Strouhal number corresponding

to periodic vortex shedding. Besides this fundamental frequency, higher harmonics appear indicating a tonal response. At $\alpha_0 = 30°$, the fundamental frequency shifts to a lower value. Multiple peaks are present, reflecting the coexistence of several interacting flow scales and the onset of nonlinear dynamics.

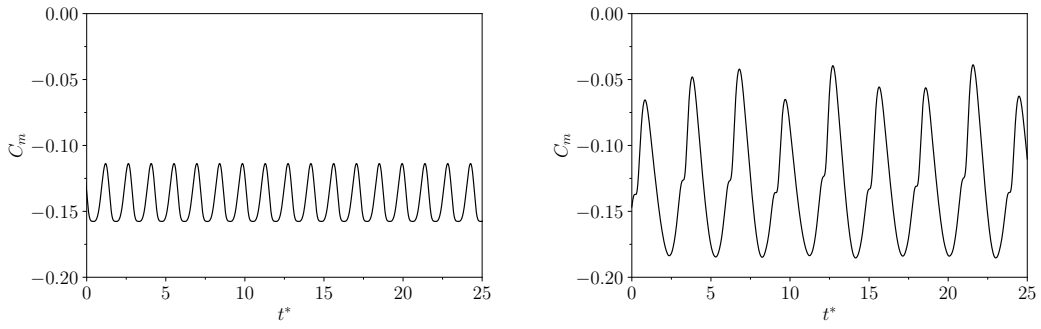


Figure 7. Time evolution of the aerodynamic moment coefficient using a common y-axis for two equilibrium angles of attack: (**a**) $\alpha_0 = 15°$ and (**b**) $\alpha_0 = 30°$.

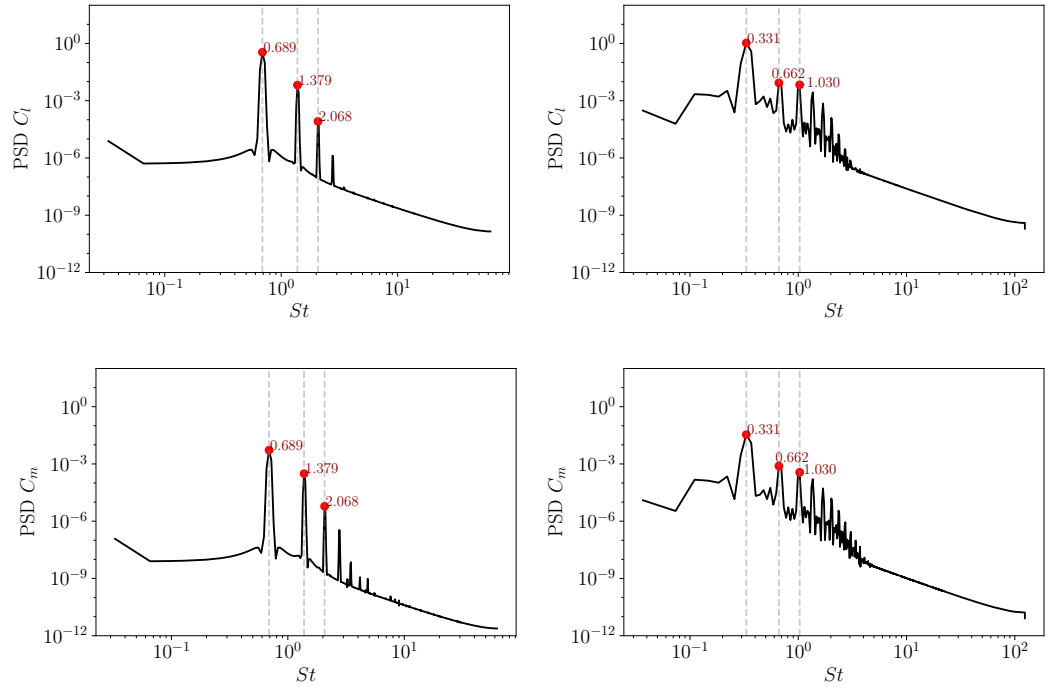


Figure 8. Power spectral density of the lift coefficient (**top row**) and moment coefficient (**bottom row**) as a function of the Strouhal number for the rigid airfoil at two equilibrium angles of attack: $\alpha_0 = 15°$ (**left column**) and $\alpha_0 = 30°$ (**right column**). The vertical dashed lines indicate the most energetic Fourier modes.

These results identify three distinct flow regimes: a steady regime at low equilibrium angle of attack, a periodic vortex-shedding regime at intermediate angles, and a strongly nonlinear separated regime at high angles. These baseline behaviors provide the reference framework for interpreting the aeroelastic response of the coupled system.

5.2. Onset of Flow-Induced Oscillations and Amplitude Response

The aeroelastic response of the system is investigated as a function of the reduced velocity U^* for different equilibrium angles of attack. The analysis focuses on the evolution

of the oscillation amplitude and the identification of the transition to large-amplitude limit-cycle oscillations.

Figure 9 shows that the system exhibits a transition from small-amplitude oscillations to large-amplitude motion as the reduced velocity increases. The critical value of U^* at which this transition occurs depends strongly on the equilibrium angle of attack. For $\alpha_0 = 0°$, the system remains stable over a wide range of reduced velocity. From this steady solution, the flow undergoes a sudden transition to large oscillations when a critical threshold is exceeded. This behavior is compatible with subcritical bifurcation, where the instability appears abruptly once a sufficient level of aerodynamic forcing is reached. A subcritical Hopf bifurcation at $\alpha_0 = 0°$ was also observed by Dimitriadis and Li [30] and Onoue et al. [19] under similar flow conditions. In contrast, for $\alpha_0 = 15°$ and 30°, the oscillation amplitude increases progressively with U^*, starting from small values and smoothly growing into the limit-cycle regime. This behavior is indicative of a supercritical bifurcation, associated with the presence of flow separation and vortex shedding already at moderate amplitudes. The equilibrium angle of attack therefore plays a key role in determining both the onset of flow-induced oscillations and the nature of the transition. Higher values of α_0 lead to an earlier onset of instability, reflecting the stronger aerodynamic forcing associated with separated-flow conditions.

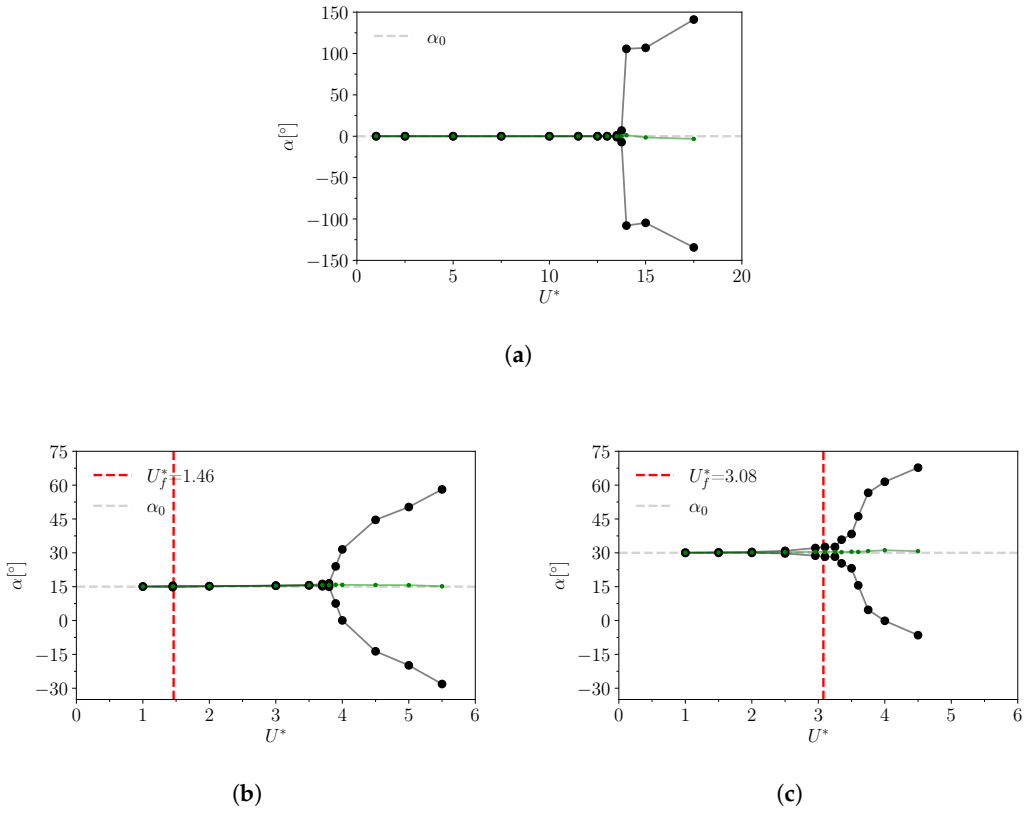
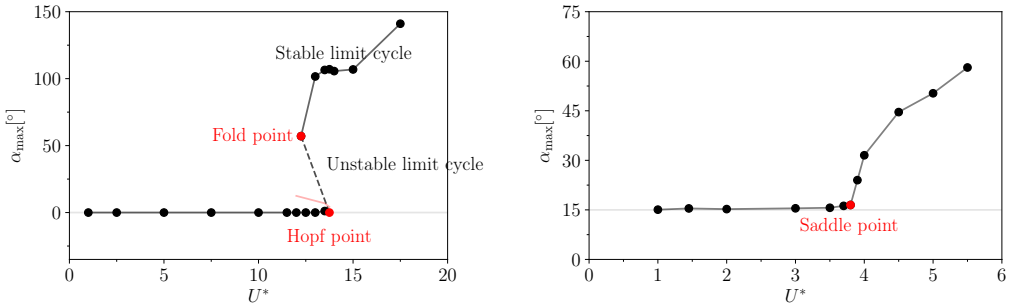


Figure 9. Maximum, minimum, and mean values of the angle of attack as a function of the reduced velocity U^* for different equilibrium angles of attack: $\alpha_0 = 0°$ (**a**), $\alpha_0 = 15°$ (**b**), and $\alpha_0 = 30°$ (**c**). The gray dashed line indicates the equilibrium angle of attack, while the red dashed line denotes the reduced velocity corresponding to the Strouhal-number peak of the associated rigid-airfoil case. The black lines represent the maximum and minimum values of the angle of attack, and the green line denotes the mean value.

The transition observed at $\alpha_0 = 0°$ is further characterized through a perturbation analysis. Specifically, an initial perturbation with maximum amplitude 10° (corresponding to approximately 10% of the maximum response amplitude) was imposed on the

angle of attack. For reduced velocities up to $U^* = 12.0$, any perturbation decays to the steady solution. Conversely, for $U^* > 12.0$, finite perturbations trigger divergence towards a limit-cycle oscillation, indicating the coexistence of stationary and oscillatory stable solutions. The perturbation amplitude was progressively reduced until the critical threshold required to trigger the limit cycle was identified for each value of U^*. The resulting bifurcation diagram reveals a finite-amplitude bistability region bounded by a Fold point ($U^* \approx 12.0$), below which all perturbations decay, and a Hopf point ($U^*_{cr} \approx 13.75$), above which infinitesimal perturbations are sufficient to trigger sustained oscillations. Furthermore, the critical perturbation amplitude decreases monotonically between the Fold and Hopf points, as shown by the red curve in Figure 10a.



(**a**) (**b**)

Figure 10. Bifurcation diagrams for $\alpha_0 = 0°$ (**a**) and $\alpha_0 = 15°$ (**b**). Black dots denote the maximum angle of attack as a function of reduced velocity, with stable solutions connected with solid lines. In panel (**a**) the dashed line indicates the unstable limit cycle and the red line indicates the critical perturbation amplitude.

Figure 10b illustrates the behavior observed at $\alpha_0 = 15°$. In this case, the stationary solution remains stable up to the critical reduced velocity ($U^* = U^*_{cr}$), beyond which, the oscillation amplitude grows continuously with increasing U^*. In addition, the results show that the mean position of the oscillation deviates slightly from the imposed equilibrium angle at low amplitudes, indicating that limit-cycle oscillations are asymmetric [19]. This behavior reflects a shift of the mean aerodynamic state prior to the onset of fully developed limit-cycle oscillations. Overall, the system exhibits two distinct transition mechanisms: a behavior consistent with a subcritical transition at low equilibrium angle of attack and a behavior consistent with a supercritical transition when separation effects become dominant. This difference in the transition topology highlights the importance of nonlinear aerodynamic effects in governing the onset of oscillations.

5.3. Frequency Coupling and Synchronization

Further insight into the aeroelastic dynamics is obtained by analyzing the frequency content of the response as a function of reduced velocity. The dominant frequencies of the pitch motion and of the aerodynamic moment are extracted and expressed in terms of the Strouhal number (St_p and St_m, respectively). The frequency analysis is performed using the stationary portion of the response after removal of the initial transient. The pitch-angle and aerodynamic-moment signals are interpolated onto a uniformly spaced time grid and analysed using Welch's method with a Hamming window. The dominant frequency is then identified as the frequency corresponding to the maximum of the power spectral density and reported in non-dimensional form as a Strouhal number.

Figure 11 shows a clear transition in the frequency response, as the reduced velocity increases. At low U^*, corresponding to high natural frequencies, the dominant frequency St_m remains nearly constant and coincides with the vortex-shedding frequency of the rigid

airfoil. In this regime, the structural motion is passively driven by the flow; the coupling between fluid and structure is weak, and the pitching oscillations occur approximately at the natural structural frequency St_n.

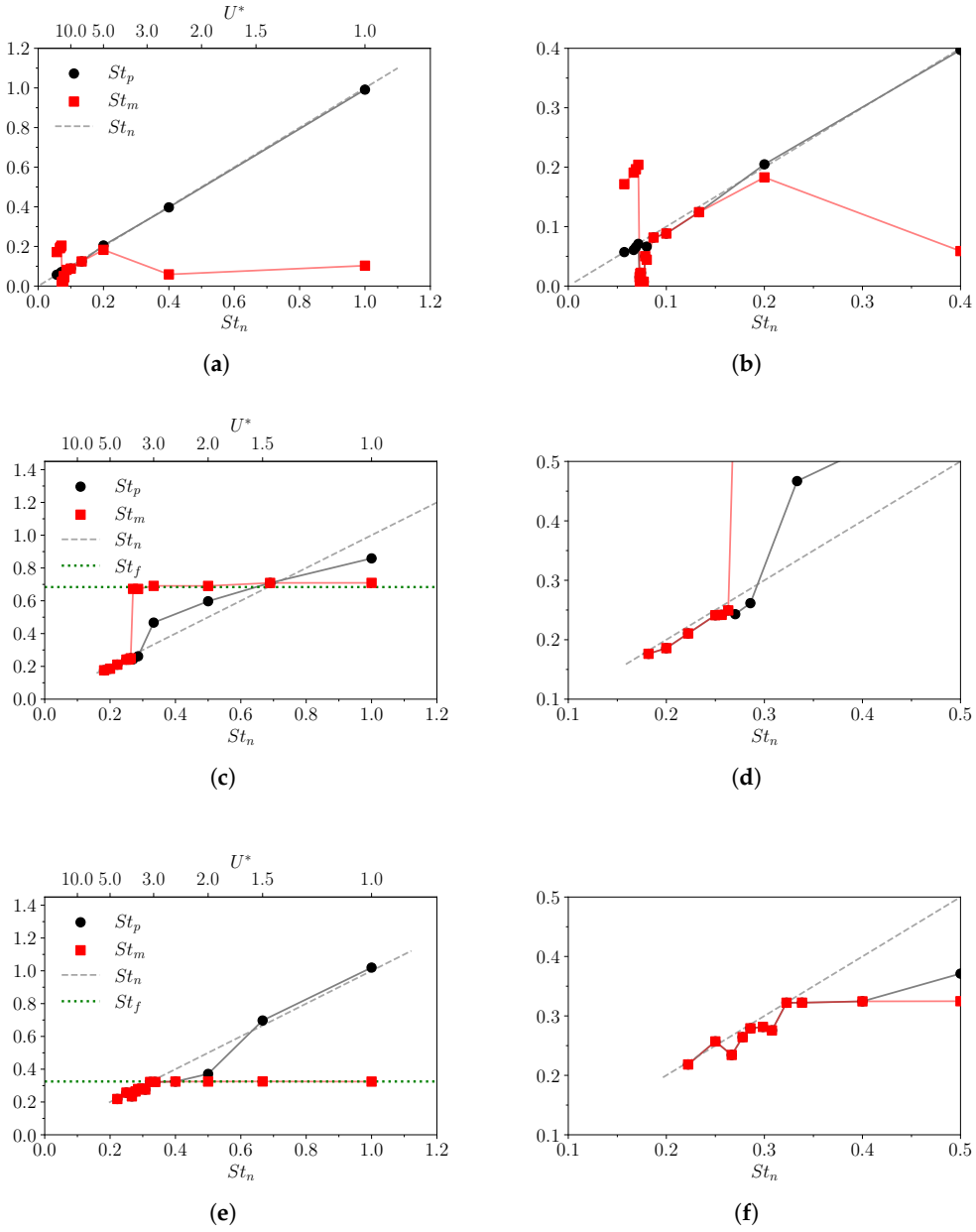


Figure 11. Peak Strouhal numbers as a function of the natural Strouhal number (St_n) for different equilibrium angles of attack: $\alpha_0 = 0°$ (**a**,**b**), $\alpha_0 = 15°$ (**c**,**d**), $\alpha_0 = 30°$ (**e**,**f**). Panels (**a**,**c**,**e**) show the full frequency range, whereas panels (**b**,**d**,**f**) focus on the low-frequency range. The black line denotes the peak Strouhal number associated with variation of the angle of attack (St_p), and the red line the peak Strouhal number associated with the moment coefficient (St_m). The gray dotted line indicates the natural Strouhal number, while the green dotted line denotes the Strouhal-number peak value for the corresponding rigid-airfoil case (St_f).

As U^* increases, an intermediate regime is observed in which multiple frequency components coexist. In addition to the vortex-shedding frequency, a lower frequency associated with the structural dynamics emerges. This regime reflects partial coupling between fluid and structure, where both mechanisms contribute to the response.

At sufficiently large U^*, the system transitions to a regime in which both St_m and St_p collapse onto a single dominant frequency corresponding to the natural frequency of the structure. In this limit-cycle regime, the aerodynamic loads and structural motion become synchronized, and the dynamics are governed by the structural response. The synchronization regime is identified by comparing the dominant frequencies extracted from the spectra of the angle of attack and moment coefficient. Frequency lock-in is assumed to occur when both signals exhibit coincident dominant spectral peaks. In several cases, higher harmonics are also observed, indicating the nonlinear nature of the oscillations.

As highlighted in the zoomed view in Figure 11b,d,f, the dominant pitching frequency is slightly lower than the natural frequency St_n. Onoue et al. [19] reported a similar behavior and attributed it to the periodic formation of a leading-edge vortex, which generates an aerodynamic torque and consequently reduces the effective stiffness and the corresponding natural frequency of the system. These results demonstrate a progressive transition from a flow-dominated regime to a fully coupled aeroelastic regime, where frequency synchronization plays a key role in the establishment of limit-cycle oscillations.

To further characterize these response regimes, representative cases for $\alpha_0 = 15^\circ$ are reported in Figure 12. In the vortex-shedding-dominated regime ($St = 0.33$), the oscillations exhibit low amplitudes and are primarily driven by the flow, with negligible structural feedback. In the marginal-stability regime ($St = 0.26$), the pitch-angle time series displays low-frequency oscillations at the natural frequency of the system, whereas the aerodynamic moment exhibits a mixed response characterized by the coexistence of low-frequency structural oscillations and higher-frequency components associated with vortex shedding, as also reported by Poirel et al. [17]. In the LCO regime ($St = 0.20$), large-amplitude oscillations develop, and the response is dominated by the structural dynamics. The flow field reveals the periodic formation and shedding of a dynamic-stall vortex during the airfoil motion. This process is reflected in the time history of the moment coefficient, where each oscillation peak is followed by a rapid drop in aerodynamic forcing. The resulting dynamics are therefore characteristic of a fully coupled aeroelastic response with strong fluid–structure interaction.

To interpret the phase relationship between the aerodynamic loads and the angular motion, a qualitative comparison is performed with the experimental results of Dimitriadis and Li [30]. The two configurations differ substantially and cannot be compared quantitatively. In the experiments, the aeroelastic response was initiated through a large externally imposed perturbation, whereas in the present simulations, the system evolves freely from the prescribed equilibrium condition. Nevertheless, the comparison is meaningful, because both studies consider large-amplitude oscillations for $\alpha_0 = 15^\circ$, with angular excursions reaching approximately 30°. Under these conditions, nonlinear aerodynamic effects, including dynamic stall, play a significant role in determining the aeroelastic response. Accordingly, the comparison is restricted to the qualitative features of the coupled dynamics.

The phase analysis reported in Figure 13 illustrates the evolution of the relationships between lift, aerodynamic moment, and angle of attack across the investigated flow conditions. The analysis is restricted to time intervals exhibiting nearly periodic behavior. Phase differences were estimated using a Fourier-based approach to ensure consistent identification of the dominant harmonic components. In the vortex-shedding-dominated regime ($St = 0.33$), sustained structural oscillations are absent, and the lift and moment coefficients remain nearly in phase, with a phase difference of approximately -17.5° (Table 3). In the marginal-stability regime ($St = 0.26$), the coexistence of multiple frequency components precludes the identification of a unique dominant frequency, consistent with the observations of Dimitriadis and Li [30], who reported alternating phase relationships. In the LCO regime ($St = 0.20$), the lift coefficient becomes nearly out of phase with the moment

coefficient. Although the structural configurations differ substantially and preclude a quantitative validation, the observed evolution of the phase relationships is in good qualitative agreement with the trends reported by Dimitriadis and Li [30].

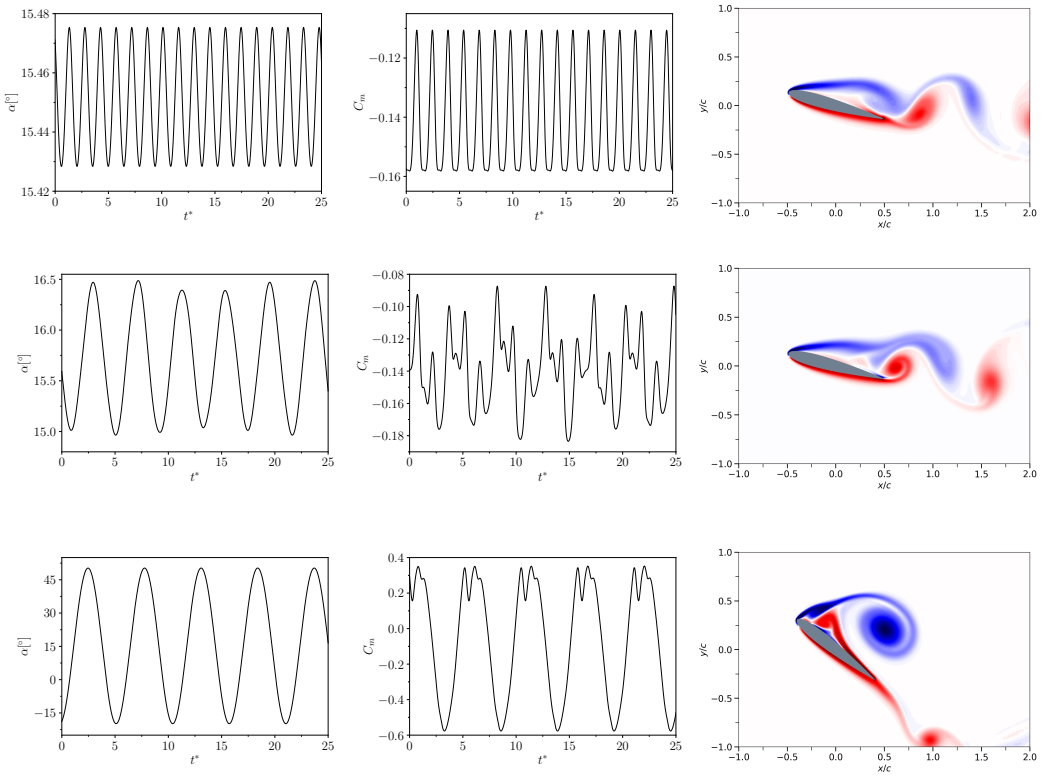
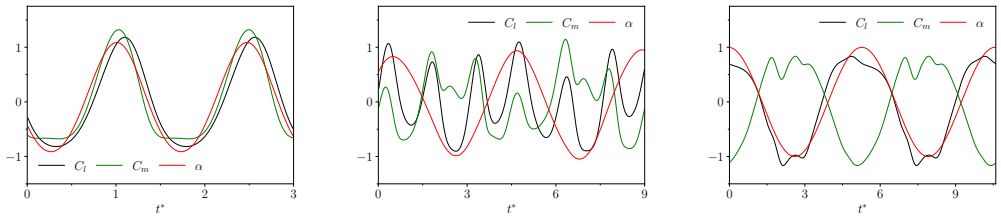


Figure 12. Time series of the angle of attack (**left column**), aerodynamic moment coefficient (**middle column**), and instantaneous vorticity contours (**right column**) for three representative response regimes: vortex-shedding-dominated ($St = 0.33$, **top row**), marginal stability ($St = 0.26$, **middle row**), and limit-cycle oscillation (LCO) ($St = 0.20$, **bottom row**). Note that the vertical axes are scaled independently in each row for clarity. The vorticity field is rendered in a colour scale ranging from blue (negative values) to red (positive values).



(**a**) (**b**) (**c**)

Figure 13. Time histories of the angle of attack, lift coefficient, and moment coefficient for the equilibrium condition $\alpha_0 = 15°$ in three representative response regimes: (**a**) vortex-shedding-dominated ($St = 0.33$), (**b**) marginal stability ($St = 0.26$), and (**c**) limit-cycle oscillation (LCO) ($St = 0.20$). To facilitate phase comparisons, each variable is normalized using its mean value and oscillation amplitude.

Table 3. Phase differences between the lift coefficient C_l, aerodynamic moment coefficient C_m, and angle of attack α for the vortex-shedding-dominated and limit-cycle-oscillation (LCO) regimes.

St	$\phi_{C_l,\alpha}$	$\phi_{C_m,\alpha}$	ϕ_{C_l,C_m}
0.33	-17.52°	0.05°	-17.57°
0.20	13.96°	-166.88°	-179.16°

5.4. Effect of Elastic-Axis Position

The influence of the elastic-axis location on the aeroelastic response is examined by comparing two configurations, corresponding to $X^*_{ec} = 0.50$ and $X^*_{ec} = 0.66$. The analysis focuses on the evolution of the oscillation amplitude as a function of reduced velocity. As shown in Figure 14, the position of the elastic axis has a significant impact on the stability threshold of the system. The critical reduced velocities reported in Table 4 provide a quantitative measure of this effect. These values were estimated from the bifurcation diagrams and should be regarded as approximate, since the simulations were performed only for discrete values of U^*. Consequently, the onset of instability can be identified only within the resolution of the sampled parameter space.

Table 4. Effect of the elastic-axis position X^*_{ec} on the onset of limit-cycle oscillations, quantified through the critical reduced velocity U^*_{crit} and its relative variation between the two elastic-axis locations, $\Delta U^* = (U^*_{crit,0.66} - U^*_{crit,0.50})/U^*_{crit,0.50}$.

α_0	U^*_{crit} (0.50)	U^*_{crit} (0.66)	ΔU^* (%)
0°	14.0	11.0	-21
15°	3.9	3.6	-7.6
30°	3.5	3.3	-5.7

In all cases, moving the elastic axis from $X^*_{ec} = 0.5$ (Figure 14a,c,e) to $X^*_{ec} = 0.66$ (Figure 14b,d,f) leads to an earlier onset of large-amplitude oscillations, corresponding to a lower critical reduced velocity. The critical reduced velocity decreases by approximately 21% for $\alpha_0 = 0^\circ$, whereas smaller reductions are observed for $\alpha_0 = 15^\circ$ and 30°. The destabilizing effect of shifting the elastic axis downstream is therefore most pronounced at low equilibrium angles of attack and progressively weakens as α_0 increases. This behavior can be attributed to the increase in the aerodynamic moment arm, which enhances the coupling between the aerodynamic forces and structural motion. As a result, the system becomes more susceptible to instability. Despite this quantitative effect, the qualitative behavior of the system remains unchanged. In particular, the nature of the transition observed for different equilibrium angles of attack is preserved. The behavior consistent with a subcritical transition at $\alpha_0 = 0^\circ$ and that consistent with a supercritical transition at higher angles are observed for both elastic-axis positions.

The frequency response follows a similar trend, with the transition from vortex-shedding-dominated behavior to synchronized aeroelastic motion occurring at lower values of reduced velocity when the elastic axis is located further downstream. These results indicate that the elastic-axis position primarily affects the stability boundaries of the system, without altering the underlying mechanisms governing the aeroelastic response.

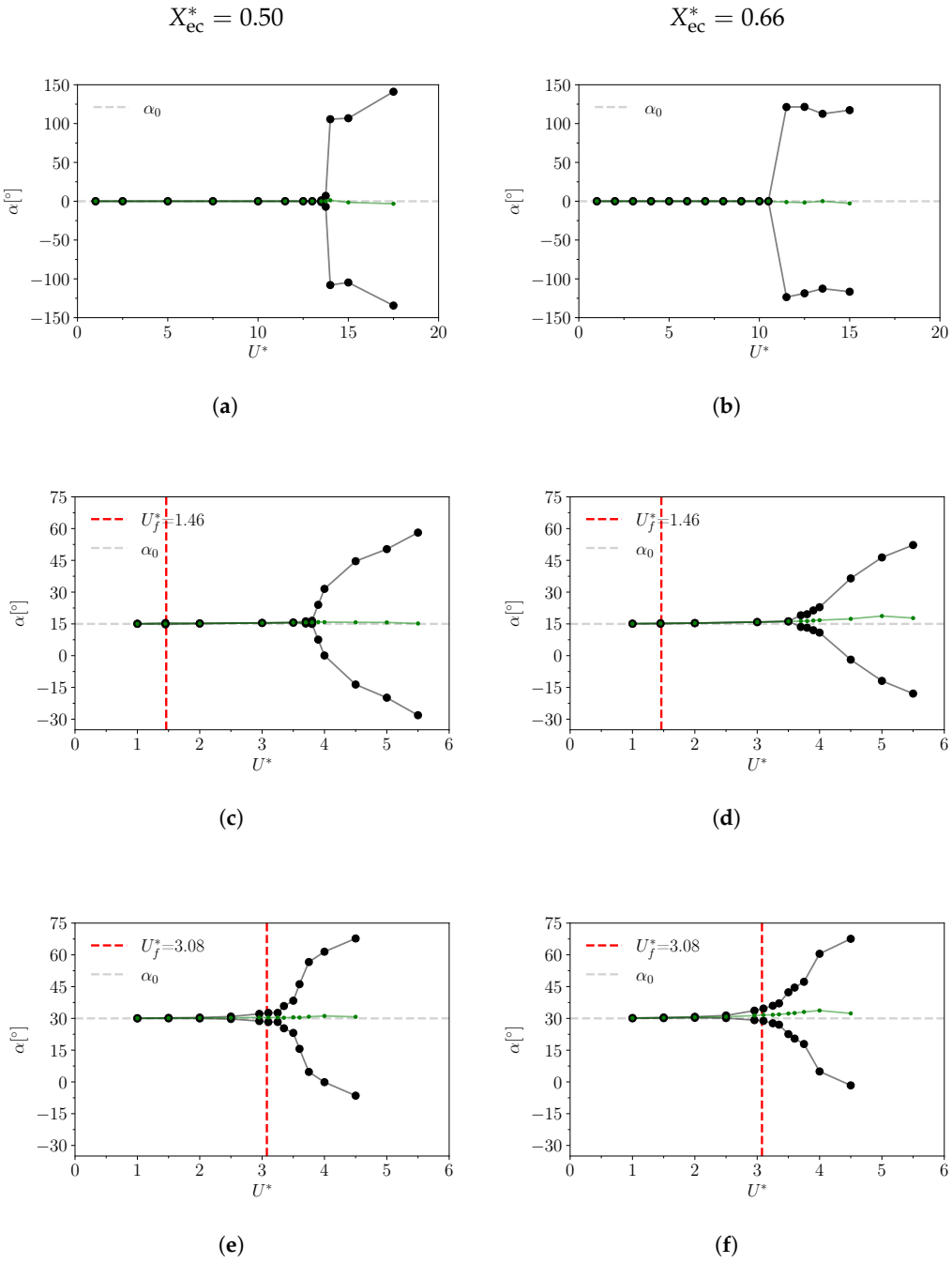


Figure 14. Maximum, minimum, and mean values of the angle of attack as a function of the reduced velocity U^* for two elastic-axis positions and for three different equilibrium angles of attack: $X^*_{ec} = 0.50$, $\alpha_0 = 0°$ (**a**), $X^*_{ec} = 0.66$, $\alpha_0 = 0°$ (**b**), $X^*_{ec} = 0.50$, $\alpha_0 = 15°$ (**c**), $X^*_{ec} = 0.66$, $\alpha_0 = 15°$ (**d**), $X^*_{ec} = 0.50$, $\alpha_0 = 30°$ (**e**), $X^*_{ec} = 0.66$, $\alpha_0 = 30°$ (**f**). The gray dashed line indicates the equilibrium angle of attack, while the red dashed line denotes the reduced velocity corresponding to the Strouhal-number peak of the associated rigid-airfoil case. The black lines represent the maximum and minimum values of the angle of attack, and the green line denotes the mean value.

6. Conclusions

The aeroelastic response of a pitching NACA0012 airfoil at low Reynolds number has been investigated through a coupled fluid–structure numerical framework based on the Navier–Stokes equations in a rotating reference frame and a single-degree-of-freedom structural model.

Although fluid-elastic instabilities and flow-induced vibrations at low Reynolds numbers have been extensively investigated, previous studies have generally focused either on the fundamental mechanisms governing stall flutter and energy transfer [3,21] or on the aeroelastic response of specific structural configurations and operating conditions [17,19]. The present work adopts a complementary perspective by systematically examining the influence of reduced velocity, equilibrium angle of attack, and elastic-axis location within a unified computational framework. Particular attention is devoted to identifying the transition from vortex-shedding-dominated oscillations to fully developed limit-cycle oscillations and to characterizing how the governing parameters modify the threshold and nature of this transition. The results provide a classification of the distinct aeroelastic regimes encountered in the system and clarify their sensitivity to both aerodynamic and structural parameters.

As a result, the analysis of the rigid airfoil highlights three distinct flow regimes as the equilibrium angle of attack increases: a steady regime at low angle, a periodic vortex-shedding regime at intermediate angles, and a strongly nonlinear separated regime at high angles. These baseline behaviors provide a reference for interpreting the aeroelastic response of the coupled system.

When structural coupling is introduced, the system exhibits a transition from small-amplitude oscillations to large-amplitude limit-cycle oscillations as the reduced velocity increases. The nature of this transition depends on the equilibrium angle of attack. A behavior consistent with a subcritical transition is observed at a low angle of attack, where oscillations appear abruptly beyond a critical threshold, whereas a behavior consistent with a supercritical transition occurs at higher angles and is characterized by a gradual growth in the oscillation amplitude.

Frequency analysis reveals a progressive transition from a flow-dominated regime, governed by vortex shedding, to a fully coupled aeroelastic regime in which the motion is synchronized with the structural natural frequency. An intermediate regime is identified, in which both flow and structural time scales contribute to the system response. The equilibrium angle of attack plays a key role in determining the onset of instability, with higher angles leading to earlier transitions and stronger aerodynamic forcing. The position of the elastic axis primarily affects the stability threshold, with downstream locations promoting an earlier onset of flow-induced oscillations, while the underlying transition mechanisms remain unchanged. Overall, the results demonstrate that flow-induced oscillations at low Reynolds number are governed by the interaction between vortex dynamics and structural response and that both aerodynamic conditions and structural parameters strongly influence the stability boundaries and dynamical regimes of the system.

The present study is restricted to two-dimensional simulations at $Re = 1000$ and therefore does not account for three-dimensional effects, transition to turbulence, or spanwise flow structures that may influence the quantitative characteristics of the response. Consequently, the results should be interpreted primarily as a characterization of the fundamental mechanisms governing the onset and development of flow-induced oscillations. Extension of the present analysis to three-dimensional flows and higher Reynolds numbers constitutes a natural direction for future research.

Author Contributions: Conceptualization, S.P., P.J. and G.S.; methodology, S.P., G.S. and M.A.C.; software, S.P. and G.S.; validation, G.S. and M.A.C.; investigation, S.P., G.S., P.J. and M.A.C.; data curation, G.S. and M.A.C.; writing—original draft preparation, M.A.C.; writing—review and editing, S.P., P.J. and G.S.; visualization, G.S. and M.A.C.; supervision, S.P. All authors have read and agreed to the published version of the manuscript.

Funding: This research was partly supported from ICSC-Centro Nazionale di Ricerca in 'High Performance Computing, Big Data and Quantum Computing', funded by European Union-NextGenerationEU. The results reported in this paper have been achieved using the EuroHPC Research Infrastructure resource LUMI supercomputer under project EHPC-REG-2025R02-307.

Institutional Review Board Statement: Not applicable.

Informed Consent Statement: Not applicable.

Data Availability Statement: The original contributions presented in the study are included in the article, further inquiries can be directed to the corresponding author.

Conflicts of Interest: The authors declare no conflicts of interest.

References

1. EASA. *Certification Specifications for Large Aeroplanes (CS-25)*; European Union Aviation Safety Agency: Cologne, Germany, 2023.
2. Bigoni, D.; Dal Corso, F.; Kirillov, O.N.; Misseroni, D.; Noselli, G.; Piccolroaz, A. Flutter instability in solids and structures, with a view on biomechanics and metamaterials. *Proc. R. Soc. A Math. Phys. Eng. Sci.* **2023**, *479*, 20230523. [CrossRef]
3. Menon, K.; Mittal, R. Flow physics and dynamics of flow-induced pitch oscillations of an airfoil. *J. Fluid Mech.* **2019**, *877*, 582–613. [CrossRef]
4. McGurk, M.; Yuan, J. Prediction and validation of aeroelastic limit cycle oscillations using harmonic balance methods and Koopman operator. *Nonlinear Dyn.* **2025**, *113*, 30841–30868. [CrossRef]
5. Baldan, G.; Guardone, A. A deep neural network reduced order model for unsteady aerodynamics of pitching airfoils. *Aerosp. Sci. Technol.* **2024**, *152*, 109345. [CrossRef]
6. Lee, T.; Gerontakos, P. Investigation of flow over an oscillating airfoil. *J. Fluid Mech.* **2004**, *512*, 313–341. [CrossRef]
7. Zhou, T.; Cao, H.; Zhao, B. Effects of Reduced Frequency on the Aerodynamic Characteristics of a Pitching Airfoil at Moderate Reynolds Numbers. *Aerospace* **2025**, *12*, 457. [CrossRef]
8. Gkiolas, D.; Mathioulakis, D. Aerodynamic study of a NACA 64418 rectangular wing under forced pitching motions. *Fluids* **2021**, *6*, 394. [CrossRef]
9. Kim, D.; Chang, J. Low-Reynolds-number effect on the aerodynamic characteristics of a pitching NACA0012 airfoil. *Aerosp. Sci. Technol.* **2014**, *32*, 162–168. [CrossRef]
10. Rezapour, S.; Mulleners, K. Dynamic stall reattachment revisited. *J. Fluid Mech.* **2026**, *1029*, A52. [CrossRef]
11. Spyropoulos, N.; Manolesoss, M.; Papadakis, G. Computational considerations for the prediction of airfoil Stall Flutter. *arXiv* **2025**, arXiv:2512.18009.
12. Liang, C.; Ou, K.; Premasuthan, S.; Jameson, A.; Wang, Z. High-order accurate simulations of unsteady flow past plunging and pitching airfoils. *Comput. Fluids* **2011**, *40*, 236–248. [CrossRef]
13. Wang, Z.; Du, L.; Zhao, J.; Thompson, M.C.; Sun, X. Flow-induced vibrations of a pitching and plunging airfoil. *J. Fluid Mech.* **2020**, *885*, A36. [CrossRef]
14. Kumar, S.; Venkatramani, J.; Gupta, A. Bifurcation and synchronization analysis in a stall-flutter aeroelastic system under varying preset angles and frequency ratios. *Sci. Rep.* **2025**, *15*, 33186. [CrossRef]
15. Yang, X.; Xu, Y.; Gao, C. Effects of Stall Pattern and Intensity on the Single-Degree-of-Freedom Aeroelastic Behavior of Airfoils. *Aerosp. Sci. Technol.* **2026**, *172*, 111720. [CrossRef]
16. Cruchaga, M.; Moreno, P. Study of stability during vortex-induced rotational vibrations at moderate Reynolds number using an immersed-boundary finite element technique. *Int. J. Numer. Methods Heat Fluid Flow* **2026**, *36*, 880–906. [CrossRef]
17. Poirel, D.; Harris, Y.; Benaissa, A. Self-sustained aeroelastic oscillations of a NACA0012 airfoil at low-to-moderate Reynolds numbers. *J. Fluids Struct.* **2008**, *24*, 700–719. [CrossRef]
18. Poirel, D.; Métivier, V.; Dumas, G. Computational aeroelastic simulations of self-sustained pitch oscillations of a NACA0012 at transitional Reynolds numbers. *J. Fluids Struct.* **2011**, *27*, 1262–1277. [CrossRef]
19. Onoue, K.; Song, A.; Strom, B.; Breuer, K. Large amplitude flow-induced oscillations and energy harvesting using a cyber-physical pitching plate. *J. Fluids Struct.* **2015**, *55*, 262–275. [CrossRef]
20. Qiu, Z.; Wang, F. Characterization of aeroelastic response and aerodynamic stiffness effect of an airfoil in the presence of dynamic stall. *Nonlinear Dyn.* **2023**, *111*, 129–154. [CrossRef]
21. Xia, Y.; Dai, Y.; Huang, G.; Yang, C. Stall flutter mitigation of an airfoil by active surface morphing. *Phys. Fluids* **2024**, *36* , 083612. [CrossRef]
22. Guo, J.; Dai, Y.; Huang, G.; Xi, Z.; Yang, C. Stall flutter prediction based on energy map by operator-network aerodynamic modeling. *AIAA J.* **2026**, *64*, 2718–2730. [CrossRef]

23. Peng, Z.; Zhu, Q. Energy harvesting through flow-induced oscillations of a foil. *Phys. Fluids* **2009**, *21*, 123602. [CrossRef]
24. Abdolahipour, S. Review on flow separation control: Effects of excitation frequency and momentum coefficient. *Front. Mech. Eng.* **2024**, *10*, 1380675. [CrossRef]
25. Michna, J.; Śledziewski, M.; Rogowski, K. The Harmonic Pitching NACA 0018 Airfoil in Low Reynolds Number Flow. *Energies* **2025**, *18*, 2884. [CrossRef]
26. Zilstra, A.; Johnson, D.A. Validated dynamic stall simulation of pitching low Reynolds number airfoils. *AIAA J.* **2024**, *62*, 3700–3712. [CrossRef]
27. Pirozzoli, S. Generalized conservative approximations of split convective derivative operators. *J. Comput. Phys.* **2010**, *229*, 7180–7190. [CrossRef]
28. Pirozzoli, S. Stabilized non-dissipative approximations of Euler equations in generalized curvilinear coordinates. *J. Comput. Phys.* **2011**, *230*, 2997–3014. [CrossRef]
29. Soldati, G.; Ceci, A.; Pirozzoli, S. FLEW: A DNS solver for compressible flows in generalized curvilinear coordinates. *Aerotec. Missili Spaz.* **2024**, *103*, 413–425. [CrossRef]
30. Dimitriadis, G.; Li, J. Bifurcation behavior of airfoil undergoing stall flutter oscillations in low-speed wind tunnel. *AIAA J.* **2009**, *47*, 2577–2596. [CrossRef]

Disclaimer/Publisher's Note: The statements, opinions and data contained in all publications are solely those of the individual author(s) and contributor(s) and not of MDPI and/or the editor(s). MDPI and/or the editor(s) disclaim responsibility for any injury to people or property resulting from any ideas, methods, instructions or products referred to in the content.